

## Article

# Phase Formation Features of Reactor Pressure Vessel Steels with Various Ni and Mn Content under Conditions of Neutron Irradiation at Increased Temperature

Evgenia Kuleshova <sup>1,2,\*</sup>, Ivan Fedotov <sup>1</sup>, Dmitriy Maltsev <sup>1</sup>, Svetlana Fedotova <sup>1</sup>, Georgiy Zhuchkov <sup>1</sup> and Alexander Potekhin <sup>1</sup>

<sup>1</sup> National Research Center “Kurchatov Institute”, Kurchatov Sq.1, 123182 Moscow, Russia; potekhin\_aa@nrcki.ru (A.P.)

<sup>2</sup> National Research Nuclear University “MEPhI”, Kashirskoe Highway 31, 115409 Moscow, Russia

\* Correspondence: evgenia-orm@yandex.ru

**Abstract:** In this paper the phase formation and mechanical properties of VVER-type reactor pressure vessel (RPV) steels with various Ni (1.57–5.95 wt.%) and Mn (0.03–0.76 wt.%) content after neutron irradiation up to fluences in the range of  $(53\text{--}120) \times 10^{22} \text{ n/m}^2$  at 400 °C were studied. The possibility of carbonitride formation under these irradiation conditions is shown. In case of sufficient Ni (>1.5 wt.%) and Mn (>0.3 wt.%) content formation of Ni-Si-Mn precipitates is observed. Their chemical composition is close to G-phase and  $\Gamma_2$ -phase and differs from that of radiation-induced precipitates in VVER-1000 RPV steels. This indicates the prerequisites for thermally conditioned mechanism of Ni-Si-Mn precipitates formation and growth at 400 °C enhanced by irradiation. It is also shown that the optimized steel manufacturing technology coupled with an ultralow Mn content ( $\leq 0.03$  wt.%) in steel with increased up to 5.26 wt.% Ni content facilitates suppressing the Ni-Si-Mn precipitates and carbonitrides formation. This, in turn, reduces the contribution of the hardening embrittlement mechanism and, correspondingly, facilitates high radiation resistance of the steels with ultralow Mn content at the increased irradiation temperature (400 °C).

**Keywords:** reactor pressure vessel (RPV) steel; high-nickel steel; mechanical properties; phase formations; radiation embrittlement mechanisms; transmission electron microscopy; atom probe tomography



**Citation:** Kuleshova, E.; Fedotov, I.; Maltsev, D.; Fedotova, S.; Zhuchkov, G.; Potekhin, A. Phase Formation Features of Reactor Pressure Vessel Steels with Various Ni and Mn Content under Conditions of Neutron Irradiation at Increased Temperature. *Metals* **2023**, *13*, 654. <https://doi.org/10.3390/met13040654>

Academic Editors: Xunxiang Hu and Weicheng Zhong

Received: 1 March 2023

Revised: 17 March 2023

Accepted: 22 March 2023

Published: 25 March 2023



**Copyright:** © 2023 by the authors. Licensee MDPI, Basel, Switzerland. This article is an open access article distributed under the terms and conditions of the Creative Commons Attribution (CC BY) license (<https://creativecommons.org/licenses/by/4.0/>).

## 1. Introduction

During operation of nuclear reactor, the material of reactor pressure vessel (low-carbon Ni-Cr-Mo-V steels) is exposed to high temperature and neutron irradiation, which leads to degradation of its structure and corresponding embrittlement [1–3]. One of the major embrittlement mechanisms during operation of VVER-type RPVs is the hardening mechanism. It results from formation of the structure elements, which act as barriers for dislocation movement in steel [1,4]. This leads to radiation hardening and, correspondingly, to radiation embrittlement of the steel [1,4]. Among the hardening structure elements formed in the RPV steels under irradiation, precipitates play a special role. The formation features of these precipitates relies heavily on the chemical composition of steels and irradiation conditions [5–7].

There are two principally distinct points of view on the reasons of Ni-Si-Mn precipitates formation in steels [8]. According to the first one, Ni-Si-Mn precipitates are formed due to radiation-induced segregation to the defect sinks (by the mechanism of the reverse Kirkendall effect), particularly dislocation loops and vacancy clusters, while precipitates themselves are not thermodynamic phases [8–11]. According to the second one, which is based on the thermodynamic models, Ni-Si-Mn precipitates are equilibrium phases,

and their formation under neutron irradiation during RPV operation is accelerated by radiation-enhanced diffusion due to the excess defects concentration [5,8,12–15].

However, largely the features of precipitate formation are considered under the typical for existing RPVs irradiation conditions with irradiation temperature not exceeding (290–300) °C. Meanwhile, the data on radiation embrittlement mechanisms for RPV steels at higher irradiation temperatures (400 °C) are almost absent, although these data might be in demand for advanced nuclear reactors, including the 4th generation reactors. Moreover, identification of the radiation embrittlement features of RPV steels at higher irradiation temperatures can contribute understanding the mechanisms of precipitate formation and radiation hardening.

Paper [8] presents the results of high dose ion irradiation of RRV steels at 400 °C, which limits their application in relation to real neutron irradiation conditions. One of the few works considering the influence of neutron irradiation at higher temperature on radiation embrittlement mechanisms in RPV steels is paper [1]. This work demonstrates the absence of Ni-Si-Mn precipitates and “black dots”-type radiation defects in the structure of 15Kh2NMFA class 1 steel after accelerated neutron irradiation at 400 °C up to fluence of  $44 \times 10^{22}$  n/m<sup>2</sup>, which are typical for lower irradiation temperature. However, the identified tendencies can be referred only to the current radiation conditions and the narrow chemical composition range. The chemical composition of RPV materials varies in a relatively wide concentration range, particularly in case of Ni and Mn. That significantly affects the features of phase formation in steel and the corresponding radiation hardening rate [5–7]. For example, the chemical composition of precipitates can vary significantly depending on Ni and Mn content in steel [7]. Furthermore, increasing the Ni content facilitates increasing the density of Ni-Si-Mn precipitates [6], and decreasing Mn content to low values (even in the case of increased Ni content) facilitates decreasing the radiation embrittlement rate due to decreasing the density of Ni-Si-Mn precipitates [16,17].

In the current work the influence of neutron irradiation at increased temperature (~400 °C) on the phase formation processes (Ni-Si-Mn precipitates particularly) in steels with various Ni and Mn content in a wide range of neutron fluences is studied. The phase formation features in the RPV steels at both typical operation temperatures of VVER-type reactors (~290–300) °C and increased irradiation temperature (~400 °C) are compared.

## 2. Materials and Methods

The RPV steels with various Ni and Mn content after accelerated irradiation at the temperature of 400 °C in the test reactor IR-8 [18] (NRC “Kurchatov institute”) up to fast neutron fluences  $(53–120) \times 10^{22}$  n/m<sup>2</sup> ( $E > 0.5$  MeV) with flux  $\sim(10^{16}–10^{17})$  n/(m<sup>2</sup>·s) were studied. Irradiation was carried out using special capsules equipped with a heater, calibrated control thermocouples, and neutron fluence activation monitors. The reliability of temperature control is confirmed by the relevant experimental and computational studies [19]. The studied materials were divided into three groups according to their Ni and Mn contents as major elements affecting the Ni-Si-Mn precipitate formation. The chemical composition (the major elements in terms of radiation embrittlement) is given in Table 1. The MM steel, that contains medium Ni and medium Mn content in terms of chemical composition is close to the conventional VVER-1000 and VVER-1200 RPVs base metal (BM) and weld metal (WM). The HL steel differs from conventional VVER-type RPV materials by high Ni and ultralow Mn content. The MM and HL materials are characterized by the enhanced strength and toughness properties and are considered as candidate materials for BM of the advanced RPVs. The HH steel has both high Ni and Mn content and represents the WM corresponding to the HL steel as BM. The copper content in all the studied steels is low enough (<0.01–0.03 wt.%), and thus Cu is not considered in the precipitate formation processes [5].

**Table 1.** Chemical composition of the studied steels.

Material Type	Chemical Composition, wt.%					
	Ni	Mn	Si	Cu	P	Fe-Cr-Mo-V-Nb-C
MM (Medium Ni, Medium Mn)	1.57	0.31	0.29	0.01	<0.005	Bal.
HL (High Ni, Low Mn)	5.26	0.03	0.11	0.02	<0.005	
HH (High Ni, High Mn)	5.95	0.76	0.15	0.04	<0.012	

Irradiation hardening was measured based on the tensile tests using cylindrical specimens with 3.0 and 1.2 mm diameter. The result processing was performed according to ISO 6892-1:2019.

Micro- and nanostructure was studied by the following methods:

- transmission electron microscopy (TEM) using the Titan 80–300 high resolution microscope (FEI, USA), equipped with energy-dispersive X-ray analysis (EDX);
- scanning electron microscopy (SEM) using the Merlin high resolution field emission scanning electron microscope (Zeiss, Germany) in radioactive shielded design, equipped with energy- and wave-dispersive analysis and Oxford Instruments electron back-scattered diffraction (EBSD) system.
- The samples were prepared by the two-side electrochemical polishing using the Struers Tenupol 5 equipment with 10% HClO<sub>4</sub> solution in methanol at the temperature below −50 °C and voltage about 20 V.
- The quantitative analysis of carbide size and number density was performed using the energy dispersive X-ray spectroscopy (EDXS) [20,21]. Selected Area Electron Diffraction (SAED) together with High Resolution TEM (HRTEM) was performed for the crystal type analysis of carbides [21]. The diffraction patterns were decoded with the use of PDF-4 X-ray database for powder diffraction and DiffraCalc software [22]. The thickness of each analyzed area was determined by the ratio of integral intensity to the zero-loss peak intensity at EELS-spectra [21] in order to calculate the number density of structural elements during TEM-observations. The size of small carbide/carbonitride phases was evaluated by TEM-images, number density—by SEM-images through recalculation from the surface density.
- The density, size and chemical composition of thermally- or radiation-induced precipitates were estimated using the CAMECA LEAP-4000 HR local electrode atom probe in the voltage mode. Atom Probe Tomography (APT) samples were prepared by the standard electropolishing method using the Simplex Electro Pointer [23]. The following ion registration parameters were used: sample temperature of 50 K, detection rate 0.15%, pulse rate 200 kHz, voltage pulse fraction 15% [23,24]. The reconstruction and data processing were performed using CAMECA IVAS 3.6.12 software. All isobar overlaps were deconvoluted by standard method in IVAS software.
- Precipitates were identified by Maximum Separation Method (MSM). All the clusters on the edge of the analyzed volume were included into overall density with the coefficient of  $\frac{1}{2}$  and their size and chemical composition were not considered. Chemical composition of precipitates was determined for cluster core by the IVAS average cluster concentration profile assuming that there were no Fe ions in the precipitates (only Ni, Mn, Si and trace amounts of P and Cu) [25].

The average size (diameter)  $D$  was estimated by the equivalent radius [26]:

$$D = 2 \left( \frac{3 V_{at} N_{ions}}{4 \pi Q} \right)^{1/3}, \quad (1)$$

where  $N_{ions}$  is the number of atoms in cluster,  $V_{at} = 0.0118 \text{ nm}^3$  is the atomic volume,  $Q$  is the detector efficiency (36% for LEAP 4000 HR).

Based on the results of mechanical tests and structural studies for various material states (fast neutron fluence), the average values of their structure and properties characteristics were obtained. Two-sample  $t$ -Test with equal variance was used to investigate the significance of differences in these average values in various states.

### 3. Results and Discussion

#### 3.1. Mechanical Test Results

The yield strength shifts for the studied steels after neutron irradiation at 400 °C up to fluences in the range of  $(53\text{--}120) \times 10^{22} \text{ n/m}^2$  were determined based on the tensile tests. Table 2 shows the corresponding yield strength shifts ( $\Delta\sigma_{0.2}$ ) for the studied steels.

**Table 2.** Yield strength shifts for the studied steels after irradiation at 400 °C.

Material Type	Chemical Elements Content, wt.%		Fast Neutron Fluence, $10^{22} \text{ n/m}^2$	Yield Strength Shift ( $\Delta\sigma_{0.2}$ ) at 22 °C, MPa
	Ni	Mn		
MM	1.57	0.31	53	$40 \pm 12$
HL	5.26	0.03	53	$16 \pm 18$
			120	$7 \pm 11$
HH	5.95	0.76	53	$64 \pm 46$
			120	$55 \pm 37$

Table 2 shows the trend towards increasing the yield strength after irradiation for all the studied steels. Meanwhile, the lowest yield strength shift at maximum fluence of  $120 \times 10^{22} \text{ n/m}^2$  was obtained for HL steel with the lowest Mn content and the highest one—for HH steel with the highest Mn content. For MM steel with medium Ni and Mn content an intermediate yield strength shift among the studied steels was obtained at maximum fluence of  $120 \times 10^{22} \text{ n/m}^2$ . The revealed radiation hardening can be associated with the changes in initial hardening carbide phases [1] and with formation of some additional barriers for dislocation movement in structure: point defect complexes (“black dots”-type dislocation loops) and Ni-Si-Mn precipitates [6]. Complex structural studies were performed to clarify the radiation hardening mechanisms.

#### 3.2. Structural Studies

##### 3.2.1. Initial Hardening Phases

Carbide phases of various types are the major initial hardening phases in the studied steels [27].

In MM and HL steels initial carbide phases are presented by [27]:

- fine (4–10) nm V- and Mo- based MC type carbides of high density;
- coarse (60–80) nm Fe- and Cr- based  $M_3C$ ,  $M_7C_3$ ,  $M_{23}C_6$  type carbides;
- coarse (60–80) nm Nb-based MC type carbides of low density.

In HH steel initial carbide phases are presented by:

- fine (5–6) nm Nb-based MC type carbides of high density;
- coarse (60–80) nm Mo- and Cr- based  $M_2C$  type carbides;
- coarse ~100 nm Fe- and Cr-based  $M_{23}C_6$  type carbides.

Changes of these carbide phases under neutron irradiation at 400 °C can change their contribution into dispersed barrier hardening, particularly due to their density increase. Figure 1 shows the parameters of initial carbide phases in the studied steels in the initial state and after irradiation at 400 °C up to  $(53\text{--}120) \times 10^{22} \text{ n/m}^2$ .

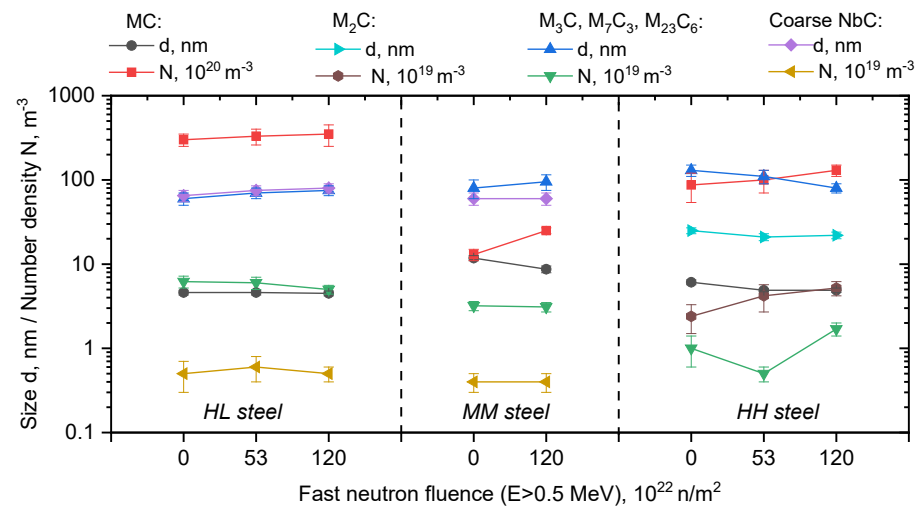


**Figure 1.** Parameters of initial carbide phases in the studied steels in the initial state and after irradiation at 400 °C up to  $(53\text{--}120) \times 10^{22} \text{ n/m}^2$ .

Figure 1 shows that there are slight differences in carbide phase parameters after irradiation in comparison with the initial state. Thus, for example, for MM and HH steels with the highest radiation hardening (see Table 2), a tendency towards increasing the density (up to 2–3 times) of fine MC type carbides and decreasing their size can be observed.

However, the revealed changes in carbide phase parameters cannot determine the observed yield strength shift. Thus, for example, changes in initial carbide phase parameters (2–3 times density increase) detected in Ref. [1] after irradiation at 400 °C in 15Kh2NMFA class 1 steel led only to 10 MPa yield strength shift, which is within the scatter. Therefore, radiation hardening of the studied steels cannot be caused by changes of initial hardening phases, but is associated with formation of some additional barriers for dislocation movement in their structure. These barriers can be: radiation defects (“black dots”-type dislocation loops) and Ni-Si-Mn precipitates, which are typical for the type and chemical composition of the considered steels [6]. Complex studies of fine structure changes were performed in order to clarify the radiation hardening mechanisms of the studied steels.

### 3.2.2. Radiation Defects—Dislocation Loops

TEM studies were performed to estimate the role of radiation defects in the revealed radiation hardening (see Table 2). Figure 2 shows the typical dark-field images of dislocation structure in dislocation loops observation conditions. Figure 2 shows that there is no evidence of radiation defects in the structure of all the studied steels after neutron irradiation at 400 °C up to the fluences  $(53\text{--}120) \times 10^{22} \text{ n/m}^2$ .

The absence of radiation defects—dislocation loops—in all the studied steels after irradiation at 400 °C is consistent with the previous studies [1]. It is associated with radiation temperature (400 °C), which is relatively high for stabilizing the point defect complexes. The absence of dislocation loops in the structure is typical for all the studied steels, since for the considered low-alloyed steels with the  $\alpha$ -Fe matrix the differences in chemical composition are insignificant in terms of formation mechanisms of radiation defect complexes.

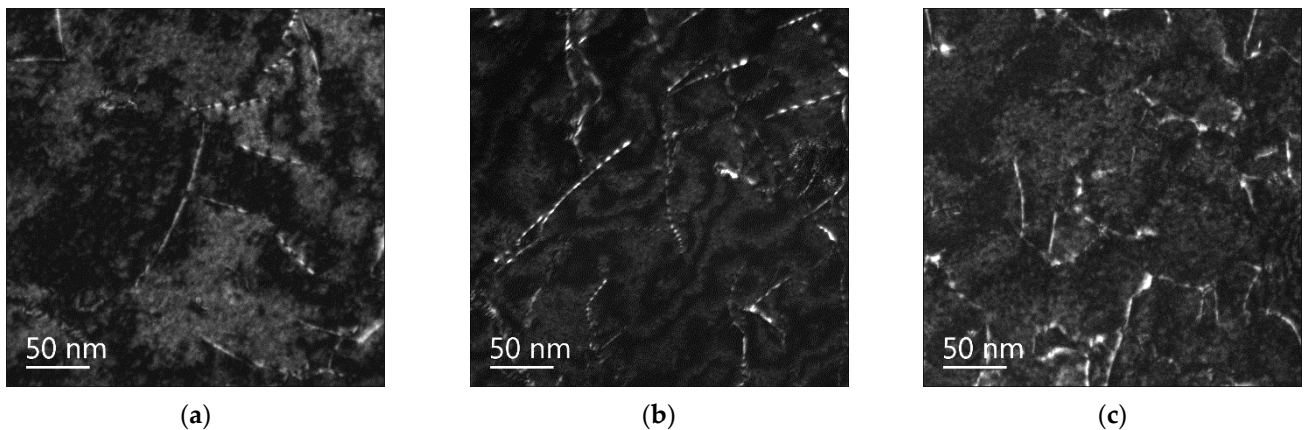


**Figure 2.** Dark-field TEM images of MM (a), HL (b) and HH (c) steels in the typical dislocation loops observation conditions after neutron irradiation at 400 °C up to  $120 \times 10^{22}$  n/m<sup>2</sup> (no loops are present).

### 3.2.3. Secondary Phase Precipitation

Numerous studies [1,4,6,9,11] showed that radiation embrittlement of the RPV steels under irradiation at operation temperature of (290–300) °C is largely caused by radiation-induced formation of Ni-Si-Mn precipitates, that nucleate on the defect cluster complexes resulting from cascade damage. It should be noted that irradiation of RPV steels at an elevated temperature (400 °C) didn't reveal formation of Ni-Si-Mn precipitates, which was attributed to the absence of stable point defect complexes due to their intense recombination. Thus, in this study formation of Ni-Si-Mn precipitates in the studied RPV steels with different contents of Ni and Mn irradiated at 400 °C was also not expected.

Complex TEM and APT studies of steels under neutron irradiation at 400 °C revealed (see Table 3):

- the absence of Ni-Si-Mn precipitates in the structure of HL steel with high Ni and ultralow Mn content;
- Ni-Si-Mn precipitates of extremely low density in the structure of MM (medium Ni, medium Mn) and HH (high Ni, high Mn) steels. A newly formed nanoscale carbonitrides that differ in size (several times less) and density (an order of magnitude higher) from the initial carbide and carbonitride phases are also observed.

The presence of Ni-Si-Mn precipitates in MM and HH steels irradiated at 400 °C in the absence of stable radiation defects was new and unexpected.

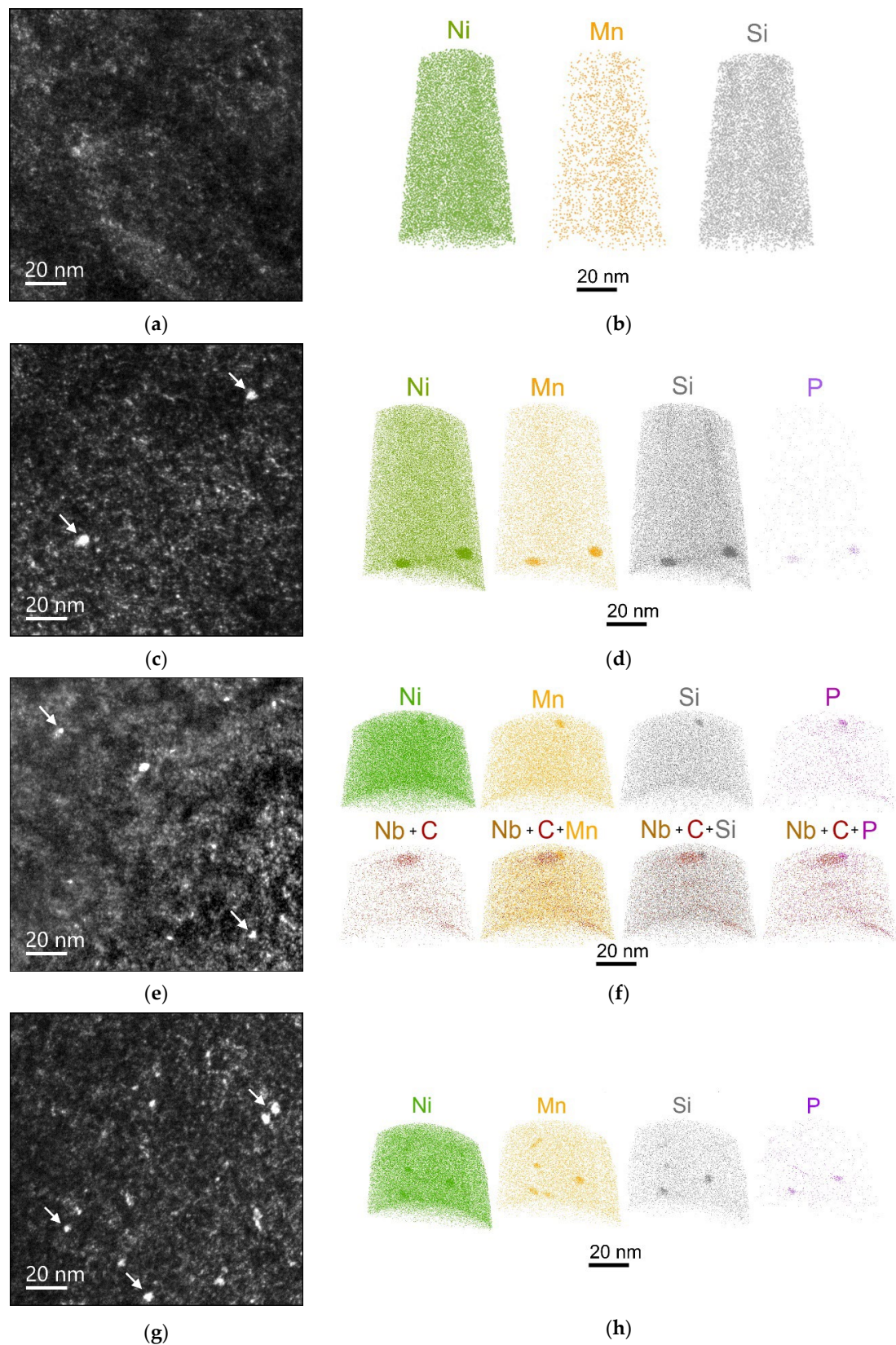
#### Ni-Si-Mn Precipitates

Figure 3 shows the typical dark-field TEM images of precipitates as well as APT maps of precipitate-forming element distribution for the studied steels. Table 3 shows the parameters (size and density) of detected precipitates in MM and HH steels. Table 4 shows the chemical composition of Ni-Si-Mn precipitates defined by APT method.

Table 3 shows that Ni-Mn-Si precipitates detected in the structure of MM and HH steels after irradiation at 400 °C are characterized by the 1.5–2 times larger size, 10–20 lower density, higher Ni and lower Si content in comparison with precipitates, previously detected in VVER-1000 RPV steels after irradiation at lower temperatures of (290–300) °C at comparable neutron fluences [6].

Table 4 shows that in HH steel with higher Mn content precipitates with higher Mn enrichment are formed, which agrees well with [7], whereas such correlation is not observed for Ni content in steels.

The differences in parameters of Ni-Si-Mn precipitates after irradiation at 400 °C in this study and at (290–300) °C in [6] can indicate the different processes of precipitates formation at 400 °C.



**Figure 3.** Typical dark-field TEM images in precipitates observation conditions (a,c,e,g) and typical APT maps of chemical element distribution (b,d,f,h) in the studied steels: HL (a,b), MM (c,d) and HH (g,h) irradiated up to fluence  $120 \times 10^{22} \text{ n/m}^2$ , and HH steel (e,f) irradiated up to fluence  $53 \times 10^{22} \text{ n/m}^2$  (arrows in TEM images indicate Ni-Si-Mn precipitates).

**Table 3.** Parameters of detected Ni-Si-Mn precipitates in MM and HH steels after neutron irradiation up to various fluences.

Steel	Fast Neutron Fluence, $10^{22} \text{ n/m}^2$	$T_{\text{irr}}$ , °C	Ni-Si-Mn Precipitates	
			d, nm (TEM/APT)	$\rho$ , $10^{22} \text{ m}^{-3}$ (TEM/APT)
SS VVER-1000 [6]	50–100	290–300	2–3	20–40
HH steel	53	400	$3.2 \pm 0.2/3.7 \pm 0.9$	$1.2 \pm 0.5/2.0 \pm 1.4$
	120		$3.4 \pm 0.2/3.8 \pm 0.8$	$1.6 \pm 0.7/2.5 \pm 1.3$
MM steel	120		$4.8 \pm 0.3/6.4 \pm 0.7$	$0.7 \pm 0.6/<1.0$

**Table 4.** Chemical composition of Ni-Si-Mn precipitates (major elements) in MM and HH steels after irradiation at 400 °C to various neutron fluences.

Steel	Fast Neutron Fluence, $10^{22} \text{ n/m}^2$	$T_{\text{irr}}$ , °C	Relative Atomic Content *, %		
			Ni	Mn	Si
SS VVER-1000 [6]	50–100	290–300	$44 \pm 5$	$21 \pm 7$	$34 \pm 8$
MM steel	120		$62 \pm 4$	$17 \pm 2$	$21 \pm 2$
HH steel	53	400	$57 \pm 19$	$32 \pm 19$	$11 \pm 10$
	120		$61 \pm 11$	$25 \pm 6$	$14 \pm 9$

\* normalized on the total Ni, Mn and Si content in precipitates.

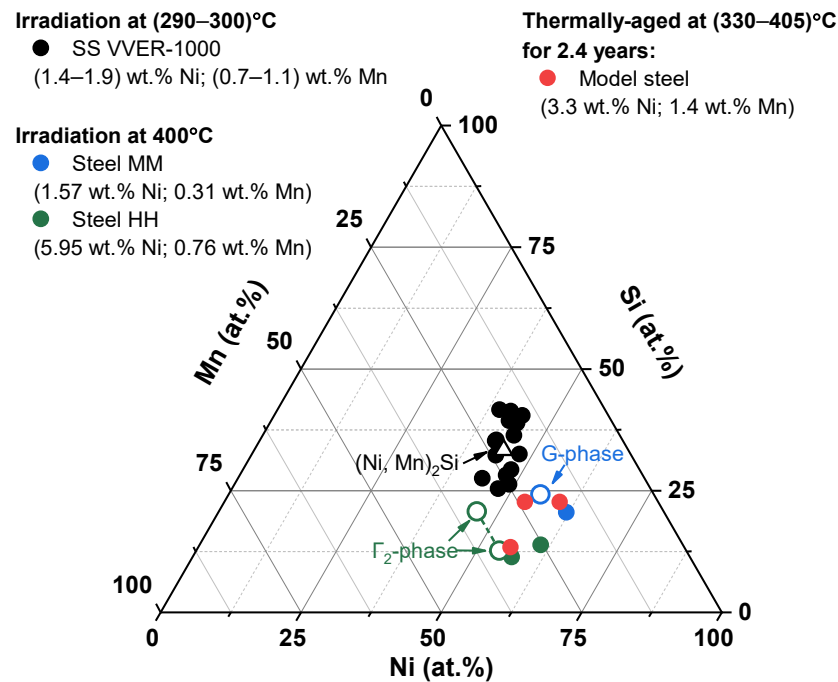
The larger size and lower density of precipitates detected in MM and HH steels in comparison with Ni-Si-Mn precipitates in VVER-1000 surveillance specimens (SS) may be associated with the increased diffusive mobility of precipitate-forming elements due to the higher irradiation temperature and higher fast neutrons fluence. This intensifies the process of precipitates growth relatively to their nucleation processes. The lower precipitates density can also be caused by lower number of their nucleation sites, which is typical for irradiation temperature of 400 °C [1].

Figure 4 shows a triple Ni-Si-Mn diagram with the marked chemical compositions of precipitates in MM and HH steels after irradiation at 400 °C together with the typical compositions of Ni-Mn-Si precipitates in VVER-1000 RPV steels after neutron irradiation at temperatures (290–300) °C, and the chemical composition of precipitates in thermally-aged model RPV steel from [13].

Figure 4 shows that for VVER-1000 RPV steels in a wide range of Ni contents and medium Mn content, chemical composition of precipitates is close to  $(\text{Ni,Mn})_2\text{Si}$  type silicides based on Ni and Mn [6], which agrees with the results of [7]. The chemical composition of Ni-Si-Mn precipitates in MM and HH steels after irradiation at 400 °C differs from the typical composition of radiation-induced Ni-Si-Mn precipitates in VVER-1000 RPV steels [6] by the higher Ni and lower Si content. It is close to the chemical composition of G-phase ( $\text{Ni}_{16}\text{Mn}_6\text{Si}_7$ , T3 [12]) in MM steel and to  $\Gamma_2$ -phase ( $(\text{Ni}_x\text{Si}_{1-x})_2\text{Mn}$ , T6 [12]) in HH steel.

It should be mentioned that paper [13] shows that Ni-Si-Mn precipitates with chemical composition close to that of G- and  $\Gamma_2$ -phase can be formed in RPV steels with high Mn content of 1.4 wt.% as a result of long-term thermal exposure of  $(20\text{--}100) \times 10^3 \text{ h}$  in the temperature range of (330–405) °C without neutron irradiation. Moreover, paper [14] shows that precipitates formed under irradiation at temperatures (290–300) °C, which are close to G- and  $\Gamma_2$ -phases in terms of composition, are coarsened under the following annealing at 425 °C through the dissolution of precipitates with the size smaller than the critical one. This precipitate behavior under annealing is noted by the authors of [14] as an evidence of the thermally conditioned nature of precipitates, which composition is close to G- and  $\Gamma_2$ -phases. Neutron irradiation in that case is an additional factor that accelerates

precipitate formation due to the enhanced diffusion and formation of additional nucleation sites.



**Figure 4.** Ni-Si-Mn triple diagram with marked areas of precipitates composition in various steels (precipitates compositions in SS VVER-1000 [6] and in thermally-aged model steel [13] are also marked).

Apparently, precipitates in HH and MM steels, which composition is close to thermodynamically stable G- and  $\Gamma_2$ -phases, correspondingly, also can have thermally conditioned nature in contrast to radiation-induced Ni-Si-Mn precipitates in VVER-1000 RPV steels after irradiation at (290–300) °C [6]. Neutron irradiation at 400 °C enhances nucleation and growth of precipitates.

Thus, despite the relatively high irradiation temperature of 400 °C, precipitate formation in the structure of steels with the typical for VVER-1000 RPVs Mn content and relatively high Ni content (>1.5 wt.%) is still possible at neutron fluences comparable to the design fluences of VVER-type RPVs. Furthermore, higher Mn and Ni content in steel leads to the increase of precipitate density, that is the higher, the higher is the accumulated fluence.

Thus, in the RPV steels under neutron irradiation at 400 °C the of Ni-Si-Mn precipitates was observed for the first time. Their chemical composition differs from that of typical Ni-Si-Mn precipitates in VVER-1000 RPV steels under irradiation at (290–300) °C and is close to G- and  $\Gamma_2$ -phases. The formation mechanism is most likely to be thermally conditioned and enhanced by irradiation. In contrast to VVER-1000 RPV steel irradiation at ~ 300 °C, where precipitates are nucleated predominantly homogeneously in the matrix, in this study interphase boundaries (the boundaries of carbide and carbonitride phases) and initial dislocations are the major nucleation sites for Ni-Si-Mn precipitates.

#### Radiation-Stimulated Carbonitrides

In addition to Ni-Si-Mn precipitates, the newly formed nanoscale carbonitride phases were detected in the studied steels under irradiation. These nanoscale carbonitrides were absent in the initial state.

Figure 5 shows typical dark-field images and typical element distribution maps of carbide and carbonitride-forming elements for the studied MM and HH steels. Table 5 shows parameters (size and density) of the detected carbonitrides in MM and HH steels.

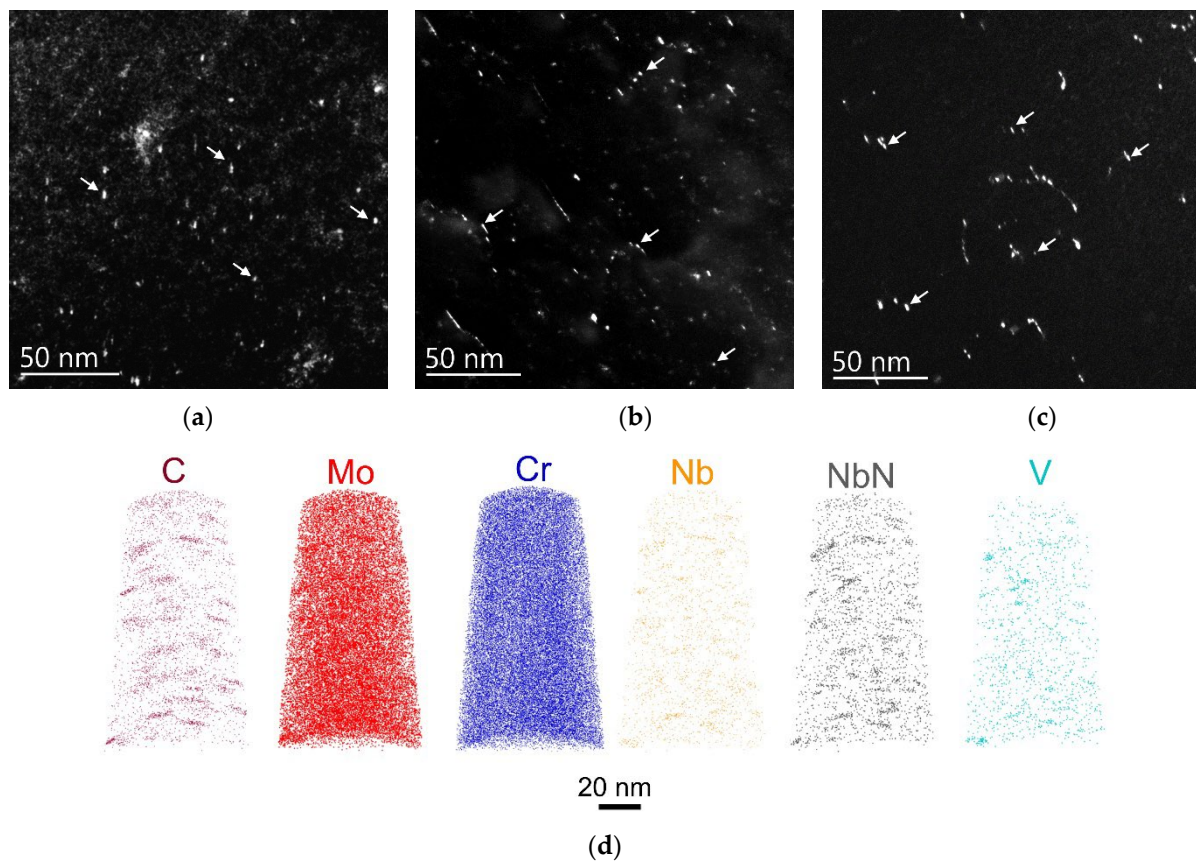


**Figure 5.** Typical dark-field TEM images of detected carbonitrides based on V, Mo and Nb after irradiation at 400 °C up to neutron fluences  $53 \times 10^{22} \text{ n/m}^2$  (b) and  $120 \times 10^{22} \text{ n/m}^2$  (a,c) in MM (a) and HH (b,c) steels, and typical APT maps of major carbide-forming elements distribution in HH steel (d) (arrows in TEM images indicate carbonitrides).

**Table 5.** Parameters of newly formed nanoscale carbonitrides detected in MM and HH steels after irradiation at 400 °C to various neutron fluences.

Steel	Fast Neutron Fluence, $10^{22} \text{ n/m}^2$	Newly Formed Carbonitrides	
		d, nm (TEM)	$\rho$ , $10^{22} \text{ m}^{-3}$ (TEM/APT)
HH	53	$1.60 \pm 0.06$	$12 \pm 7/18 \pm 6$
	120	$1.97 \pm 0.08$	$4 \pm 2/13 \pm 7$
MM	120	$2.04 \pm 0.13$	$6 \pm 4$

APT analysis revealed formation of two types of carbonitride phases under irradiation: Larger phases with disk-shaped morphology and atomic ratio of elements 60Nb-20Mo-15Cr-5V-CN;

Smaller phases with spherical morphology and atomic ratio of elements 40Cr-30Mo-25Nb-5V-CN.

Meanwhile, no changes in chemical composition of carbonitrides were observed after increasing the irradiation fluence.

Table 5 shows that in HH steel the average size of carbonitrides increases and their number density decreases with the neutron fluence increase. This is typical for phase formation process and can indicate the influence of radiation-enhanced diffusion on carbonitrides formation and growth processes. The APT obtained values of carbonitride average size are in good agreement with the data set obtained by TEM (see Figure 6).

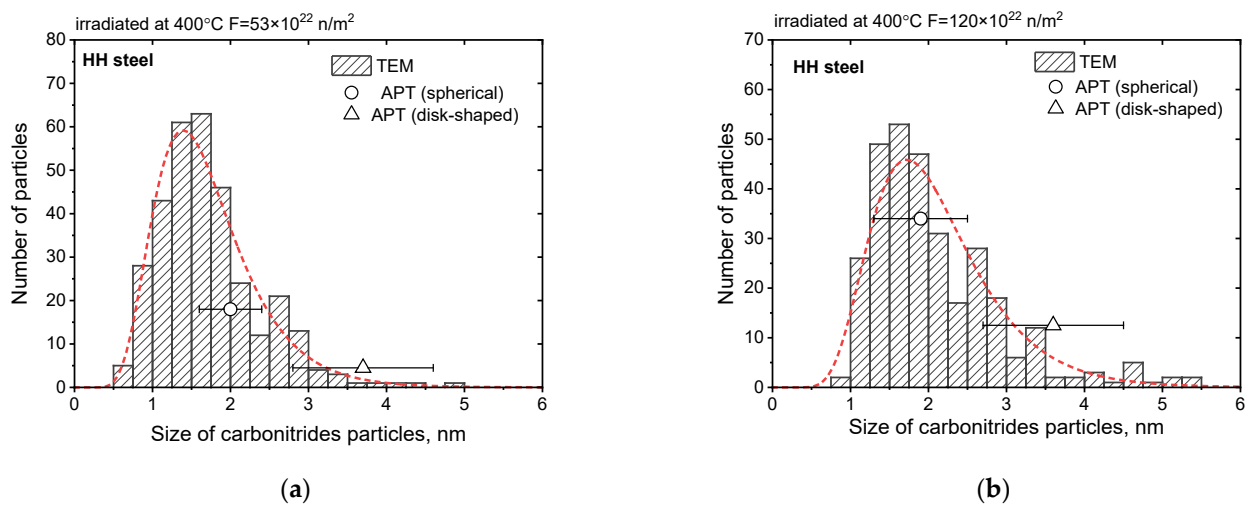


**Figure 6.** Size distribution histograms for the Nb, Mo and V-based carbonitrides detected in HH steel after irradiation at 400 °C up to fast neutron fluences  $53 \times 10^{22} \text{ n/m}^2$  (a) and  $120 \times 10^{22} \text{ n/m}^2$  (b).

Carbonitride formation in MM and HH steels after irradiation at 400 °C is caused by the partial dissolution of initial carbide and carbonitride phases (see Figure 1) and the following formation of new phases. This is manifested in the density increase of initial phases and their size decrease, which was observed earlier in [1]. The process of carbonitride formation may be driven by the features of chemical composition (the ratio of carbide- and nitride-forming elements content to C and N content) and the standard heat-treatment mode. Thus, for example, in HL steel, which has undergone a set of optimization steps to increase its structural stability (chemical composition and heat-treatment mode optimization), no evidence of carbonitride formation was detected after irradiation at 400 °C despite the similar content of carbide-forming elements.

### 3.2.4. Evaluation of the Contribution from the Structure Changes into Radiation Hardening

As it was shown earlier (see Table 2), a yield strength increase after irradiation was revealed for all the studied steels. This indicates the formation of new barriers for dislocation motion in the steel structure. The structural studies showed the presence of Ni-Si-Mn precipitates and nanoscale carbonitrides based on Cr, Mo and Nb in the structure of MM and HH steels, which were absent in the initial steel structure. They might lead to radiation hardening of the studied steels. However, no structure changes were detected for HL steel, while the minor observed changes of the yield strength are apparently associated with the property's value scatter.

For HH and MM steels the detected increase of the yield strength is referred to the formation of Ni-Si-Mn precipitates and nanoscale carbonitrides in the steel structure. The contribution of the observed structural components into radiation hardening was assessed in accordance with the dispersed barrier hardening model by the equation [6,28]:

$$\sigma_{0.2} = \sqrt{\sum \sigma_i^2}, \quad (2)$$

where  $\sigma_i$  is contribution from the structural components (barriers) of similar type. It is determined by the following equation [6,28–30]:

$$\sigma_i = \alpha M G b \sqrt{N_i d_i}, \quad (3)$$

where  $\alpha$  is a coefficient that characterizes the barrier strength for the current structural component,  $M = 2.75$  is Taylor factor,  $G = 81 \text{ GPa}$  is the shear modulus,  $b = 0.248 \text{ nm}$  is a Burgers vector,  $N_i$  is the number density of the structural components of the current type,  $d_i$  is an average size of the structural components of the current type.

The contribution into the additional dispersed hardening from Ni-Si-Mn precipitates and carbonitrides was estimated with the use of the coefficient  $\alpha = 0.08$ , which was previously used for estimation of Ni-Si-Mn precipitates hardening contribution [6,29,30].

Figure 7 shows the dose dependencies of radiation hardening for the studied steels with the marked experimental and calculated by Equations (2) and (3) values. Figure 7 also shows the dose dependence of yield strength change after irradiation at  $T = (290\text{--}300)^\circ\text{C}$  for WM VVER-1000 RPVs with medium Ni and high Mn content [6].

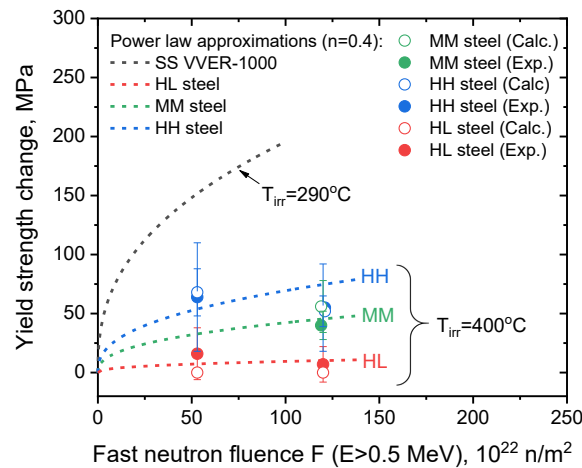


**Figure 7.** Experimental (filled symbols) and calculated (open symbols) yield strength shifts for the studied steels and for SS VVER-1000 [6] (dashed lines show power law approximations with the degree index  $n = 0.4$ ).

Figure 7 shows a good agreement between the experimental and calculated data of radiation hardening. Thus, for example, for HH steel the calculated yield strength shifts show the similar to experimental data tendency of lower radiation hardening at higher neutron fluence. This is associated with the formation and coarsening of V, Mo, Cr and Nb-based carbonitrides with their density decrease, which was detected by the structural studies (see Table 5).

Furthermore, the revealed radiation hardening for the studied steels are significantly lower than the typical values for WM VVER-1000 RPVs at comparable fluences but lower irradiation temperature. This should facilitate lower radiation embrittlement, *ceteris paribus*. It should be noted that the hardening contribution of carbonitride phases in HH and MM steels is somewhat higher in comparison with Ni-Si-Mn precipitates due to the lower density of the latter. Meanwhile, it is worth considering that radiation defects—dislocation loops with the significantly higher barrier strength coefficient  $\alpha = 0.33$  [6] are absent. This also facilitates the lower radiation embrittlement rate. Thus, on the example of HL steel it can be seen that suppression of the carbonitride formation due to optimization of the chemical composition and heat-treatment mode can enable a significant reduction of radiation hardening effects and, correspondingly, radiation embrittlement effects at radiation temperature of  $400^\circ\text{C}$ . Decreasing the Mn content in steel, in its turn, facilitates almost total suppression of the steel radiation hardening at  $400^\circ\text{C}$  through the absence of Ni-Si-Mn precipitates even at increased Ni content in steel. This can be also seen on the example of HL steel.

#### 4. Conclusions

Studies of the RPV steels with various Ni and Mn content (in the Ni range (1.57–5.95 wt.%) and Mn range (0.02–0.76 wt.%) after neutron irradiation at  $400^\circ\text{C}$  in the fast fluence range  $(53\text{--}120) \times 10^{22} \text{ n/m}^2$  revealed that:

- Ni-Si-Mn precipitates formation at  $400^\circ\text{C}$  is possible under neutron irradiation in RPV steels with Ni content 1.57 and 5.95 wt.% and sufficient Mn content  $> 0.3 \text{ wt.}\%$ ;

- Ni-Si-Mn precipitates formation is possible in RPV steels at 400 °C even in the absence of radiation defects—dislocation loops (as their preferable nucleation sites), apparently at sufficient Mn content in steel;
- Ni-Si-Mn precipitates formed in the studied steels under irradiation at 400 °C differ in terms of chemical composition from radiation-induced precipitates formed at 290 °C in VVER-1000 RPV materials;
- Ni-Si-Mn precipitates formed in the studied steels irradiated at 400 °C in terms of chemical composition are close to thermodynamically stable G-phase and  $\Gamma_2$ -phase and have the features of thermally conditioned nucleation and growth mechanism, which is enhanced by neutron irradiation;
- at the increased irradiation temperature of 400 °C formation of carbonitride phases with high density is detected in the studied steels with Ni content 1.57 and 5.95 wt.% and Mn content > 0.3 wt.%, particularly due to re-dissolution of the initial hardening phases. This is not observed in the steel with high Ni (5.26 wt.%) and ultralow Mn ( $\leq 0.03$  wt.%) content due to the optimized chemical composition and heat-treatment mode;
- the ultralow Mn content ( $\leq 0.03$  wt.%) in the steel with high Ni (5.26 wt.%) content facilitates suppression of Ni-Si-Mn precipitates formation under irradiation at 400 °C. This ensures high radiation resistance of the RPV steels with ultralow Mn content due to the absence of the hardening embrittlement mechanism at the increased irradiation temperature (400 °C).

**Author Contributions:** E.K.: Conceptualization, supervision, methodology, writing—original draft; I.F.: formal analysis, investigation (transmission electron microscopy), visualization, writing—review & editing; D.M.: investigation (scanning electron microscopy observations), discussing; S.F.: investigation (atom probe tomography observations), discussing, writing—review & editing; G.Z.: investigation (atom probe tomography observations), visualization; A.P.: investigation (atom probe tomography observations), visualization, writing—review & editing. All authors have read and agreed to the published version of the manuscript.

**Funding:** This research received no external funding.

**Data Availability Statement:** The data presented in this study are available upon request from the corresponding author.

**Conflicts of Interest:** The authors declare no conflict of interest.

## References

1. Kuleshova, E.A.; Gurovich, B.A.; Bukina, Z.V.; Frolov, A.S.; Maltsev, D.A.; Krikun, E.V.; Zhurko, D.A.; Zhuchkov, G.M. Mechanisms of Radiation Embrittlement of VVER-1000 RPV Steel at Irradiation Temperatures of (50–400)°C. *J. Nucl. Mater.* **2017**, *490*, 247–259. [[CrossRef](#)]
2. Odette, G.R.; Yamamoto, T.; Williams, T.J.; Nanstad, R.K.; English, C.A. On the History and Status of Reactor Pressure Vessel Steel Ductile to Brittle Transition Temperature Shift Prediction Models. *J. Nucl. Mater.* **2019**, *526*, 151863. [[CrossRef](#)]
3. Margolin, B.Z.; Nikolayev, V.A.; Yurchenko, E.V.; Nikolayev, Y.A.; Erak, D.Y.; Nikolayeva, A.V. Analysis of Embrittlement of WWER-1000 RPV Materials. *Int. J. Press. Vessel. Pip.* **2012**, *89*, 178–186. [[CrossRef](#)]
4. Castin, N.; Bonny, G.; Konstantinović, M.J.; Bakaev, A.; Bergner, F.; Courilleau, C.; Domain, C.; Gómez-Ferrer, B.; Hyde, J.M.; Messina, L.; et al. Multiscale Modelling in Nuclear Ferritic Steels: From Nano-Sized Defects to Embrittlement. *Mater. Today Phys.* **2022**, *27*, 100802. [[CrossRef](#)]
5. Wells, P.B.; Yamamoto, T.; Miller, B.; Milot, T.; Cole, J.; Wu, Y.; Odette, G.R. Evolution of Manganese–Nickel–Silicon-Dominated Phases in Highly Irradiated Reactor Pressure Vessel Steels. *Acta Mater.* **2014**, *80*, 205–219. [[CrossRef](#)]
6. Kuleshova, E.A.; Zhuchkov, G.M.; Fedotova, S.V.; Maltsev, D.A.; Frolov, A.S.; Fedotov, I.V. Precipitation Kinetics of Radiation-Induced Ni-Mn-Si Phases in VVER-1000 Reactor Pressure Vessel Steels under Low and High Flux Irradiation. *J. Nucl. Mater.* **2021**, *553*, 22–26. [[CrossRef](#)]
7. Almirall, N.; Wells, P.B.; Yamamoto, T.; Wilford, K.; Williams, T.; Riddle, N.; Odette, G.R. Precipitation and Hardening in Irradiated Low Alloy Steels with a Wide Range of Ni and Mn Compositions. *Acta Mater.* **2019**, *179*, 119–128. [[CrossRef](#)]
8. Almirall, N.; Wells, P.B.; Pal, S.; Edmondson, P.D.; Yamamoto, T.; Murakami, K.; Odette, G.R. The Mechanistic Implications of the High Temperature, Long Time Thermal Stability of Nanoscale Mn-Ni-Si Precipitates in Irradiated Reactor Pressure Vessel Steels. *Scr. Mater.* **2020**, *181*, 134–139. [[CrossRef](#)]

9. Konstantinović, M.J.; Uytendhouwen, I.; Bonny, G.; Castin, N.; Malerba, L.; Efsing, P. Radiation Induced Solute Clustering in High-Ni Reactor Pressure Vessel Steel. *Acta Mater.* **2019**, *179*, 183–189. [[CrossRef](#)]
10. Ngayam-Happy, R.; Becquart, C.S.; Domain, C.; Malerba, L. Formation and Evolution of MnNi Clusters in Neutron Irradiated Dilute Fe Alloys Modelled by a First Principle-Based AKMC Method. *J. Nucl. Mater.* **2012**, *426*, 198–207. [[CrossRef](#)]
11. Ke, J.H.; Spencer, B.W. Cluster Dynamics Modeling of Mn-Ni-Si Precipitates Coupled with Radiation-Induced Segregation in Low-Cu Reactor Pressure Vessel Steels. *J. Nucl. Mater.* **2022**, *569*, 153910. [[CrossRef](#)]
12. Xiong, W.; Ke, H.; Krishnamurthy, R.; Wells, P.; Barnard, L.; Odette, G.R.; Morgan, D. Thermodynamic Models of Low-Temperature Mn–Ni–Si Precipitation in Reactor Pressure Vessel Steels. *MRS Commun.* **2014**, *4*, 101–105. [[CrossRef](#)]
13. Jenkins, B.M.; Styman, P.D.; Riddle, N.; Bagot, P.A.J.; Moody, M.P.; Smith, G.D.W.; Hyde, J.M. Observation of Mn-Ni-Si-Rich Features in Thermally-Aged Model Reactor Pressure Vessel Steels. *Scr. Mater.* **2021**, *191*, 126–130. [[CrossRef](#)]
14. Almirall, N.; Wells, P.B.; Ke, H.; Edmondson, P.; Morgan, D.; Yamamoto, T.; Odette, G.R. On the Elevated Temperature Thermal Stability of Nanoscale Mn-Ni-Si Precipitates Formed at Lower Temperature in Highly Irradiated Reactor Pressure Vessel Steels. *Sci. Rep.* **2019**, *9*, 9587. [[CrossRef](#)] [[PubMed](#)]
15. Ke, H.; Wells, P.; Edmondson, P.D.; Almirall, N.; Barnard, L.; Odette, G.R.; Morgan, D. Thermodynamic and Kinetic Modeling of Mn-Ni-Si Precipitates in Low-Cu Reactor Pressure Vessel Steels. *Acta Mater.* **2017**, *138*, 10–26. [[CrossRef](#)]
16. Stofanek, R.J.; Poskie, T.J.; Li, Y.Y.; Wire, G.L. Irradiation Damage Behavior of Low Alloy Steel Wrought and Weld Materials. In Proceedings of the the Sixth International Symposium on Environmental Degradation of Materials in Nuclear Power Systems—Water Reactors, San Diego, CA, USA, 1–5 August 1993; p. 10.
17. Lee, B.S.; Kim, M.C.; Yoon, J.H.; Hong, J.H. Characterization of High Strength and High Toughness Ni-Mo-Cr Low Alloy Steels for Nuclear Application. *Int. J. Press. Vessel. Pip.* **2010**, *87*, 74–80. [[CrossRef](#)]
18. Ryazantsev, E.P.; Egorenkov, P.M.; Yashin, A.F. Operation of the IR-8 Reactor with IRT-3M Type Fuel Assemblies. *Nucl. Eng. Des.* **1998**, *182*, 241–247. [[CrossRef](#)]
19. Trofimchuk, V.V.; Nasonov, V.A.; Erak, D.Y.; Pesnya, Y.E.; Kruglikov, A.E.; Mikhin, O.V. Determination of Energy Release from Gamma Radiation in Experimental Channels of the IR-8 Reactor. *Probl. Nucl. Sci. Eng. Ser. Phys. Nucl. React.* **2022**, *5*, 20–29.
20. Bell, D.C.; Garratt-Reed, A.J. *Energy Dispersive X-ray Analysis in the Electron Microscope*; Microscopy Handbooks; Taylor & Francis: Oxford, UK, 2003; p. 160C. ISBN 9780203483428.
21. Williams, D.B.; Carter, C.B. *Transmission Electron Microscopy: A Textbook for Materials Science*; Cambridge Library Collection; Springer: New York, NY, USA, 2009.
22. Frolov, A.S.; Krikun, E.V.; Prikhodko, K.E.; Kuleshova, E.A. Development of the DIFFRACALC Program for Analyzing the Phase Composition of Alloys. *Crystallogr. Rep.* **2017**, *62*, 809–815. [[CrossRef](#)]
23. Larson, D.J.; Prosa, T.J.; Ulfing, R.M.; Geiser, B.P.; Kelly, T.F. *Local Electrode Atom Probe Tomography*; Springer Science: New York, NY, USA, 2013; ISBN 978-1-4614-8720-3.
24. Miller, M.K.; Forbes, R.G. *Atom-Probe Tomography*; Springer US: Boston, MA, USA, 2014; ISBN 978-1-4899-7429-7.
25. Edmondson, P.D.; Parish, C.M.; Nanstad, R.K. Using Complimentary Microscopy Methods to Examine Ni-Mn-Si-Precipitates in Highly-Irradiated Reactor Pressure Vessel Steels. *Acta Mater.* **2017**, *134*, 31–39. [[CrossRef](#)]
26. Styman, P.D.; Hyde, J.M.; Wilford, K.; Parfitt, D.; Riddle, N.; Smith, G.D.W. Characterisation of Interfacial Segregation to Cu-Enriched Precipitates in Two Thermally Aged Reactor Pressure Vessel Steel Welds. *Ultramicroscopy* **2015**, *159*, 292–298. [[CrossRef](#)]
27. Kuleshova, E.A.; Fedotov, I.V.; Maltcev, D.A.; Potekhin, A.A.; Bubyakin, S.A.; Isaenkova, M.G.; Krymskaya, O.A.; Minushkin, R.A. Structural Features Ensuring the Increase of Service Characteristics of High-Nickel Steels for Pressure Vessels of Prospective Energy-Generation Reactors. *Int. J. Press. Vessel. Pip.* **2022**, *200*, 104845. [[CrossRef](#)]
28. Kuleshova, E.A.; Fedotov, I.V. Annealing as a Technique for Estimating the Structural Elements Contribution to NPP Materials Service Properties. *Phys. Met. Metallogr.* **2019**, *120*, 763–769. [[CrossRef](#)]
29. Kuleshova, E.A.; Gurovich, B.A.; Lavrukhina, Z.V.; Maltsev, D.A.; Fedotova, S.V.; Frolov, A.S.; Zhuchkov, G.M. Study of the Flux Effect Nature for Vver-1000 RPV Welds with High Nickel Content. *J. Nucl. Mater.* **2017**, *483*, 1–12. [[CrossRef](#)]
30. Lambrecht, M.; Al, E. On the Correlation between Irradiation-Induced Microstructural Features and the Hardening of Reactor Pressure Vessel Steels. *J. Nucl. Mater.* **2010**, *406*, 84–89. [[CrossRef](#)]

**Disclaimer/Publisher’s Note:** The statements, opinions and data contained in all publications are solely those of the individual author(s) and contributor(s) and not of MDPI and/or the editor(s). MDPI and/or the editor(s) disclaim responsibility for any injury to people or property resulting from any ideas, methods, instructions or products referred to in the content.